Ion Optics Calculations for Tritium Injection into JET

P. Kirby
A. P. H. Goede
S. Papastergiou

UK ATOMIC ENERGY
AUTHORITY

Culham
Laboratory

Ion Optics Calculations for
Tritium Injection into JET

P. Kirby

Culham Laboratory, Abingdon, Oxfordshire, OX14 3DB, UK

(Euratom/UKAEA Fusion Association)

A.P.H. Goede†, S. Papastergiou

JET Joint Undertaking, Abingdon, Oxfordshire, OX14 3EA, UK

†*now at SRON, Utrecht, The Netherlands*

Abstract

An account is given of the numerical ion optics calculations that have been performed for the proposed injection of 160 keV tritium beams into JET. A feature of this work is the representation of the field of the beam deflection magnet by an analytic Laplacian function based on detailed experimental measurements. A practical approach to the problem of calculating the surface power density in the ion beam dump has allowed extensive results to be obtained simply, despite the complicated geometry.

1. Introduction

The Joint European Torus (JET) is a large toroidal device in which it is hoped to demonstrate the controlled thermonuclear fusion of deuterium and tritium and establish its potential as a future source of energy. Initiation of the fusion reaction requires a very high temperature, and it is necessary to use additional heating, usually by the injection of high-energy neutral beams or electromagnetic waves, or both.

JET has so far operated without tritium and its neutral injection system is designed for 140 keV, 30 A deuterium beams. For the tritium phase of operation, there is a definite advantage in injecting tritium itself, because this serves to maximize its concentration in the centre of the machine, where the temperature is highest. It is therefore of importance to know whether the existing injection system can be converted to operate with tritium (160 keV, 30 A). It is to this question that the present work is addressed.

The specific area of interest concerns the deflection magnet used to separate out the residual un-neutralized component of each beam after neutralization, and to steer it into an actively cooled beam dump. Owing to the relatively low neutralization efficiency, this ion component is rather large (typically 2.25 MW for each ion source), and it would otherwise be deflected by the magnetic fields in JET itself onto material unable to withstand the thermal load.

Operational experience with the deflection magnets now exists for hydrogen and deuterium beams [1,2], and this has allowed validation of the original beam optics calculations carried out during the design phase of the magnet [3]. Also, effects not quantified in these previous calculations, such as the experimentally observed space-charge effects [2] have been assessed. Subsequent modifications to the ion beam dump in order to enhance its beam acceptance are incorporated into this paper.

For the proposed tritium operation of the JET neutral injector, it is important to emphasize that retrospective modification of the system will not again be possible, owing to the induced radioactivity of the mechanical components. High reliability of the predicted ion optics of the magnet and the subsequent calculation of the power density distribution on the ion dump is therefore paramount. The approach adopted here is to make use of measured magnetic field values, rather than the numerically obtained values used previously, as the latter have been shown to be of insufficient accuracy to represent the fringe field of the magnet, in particular under the prevailing condition of high saturation [4].

The procedure is to calculate the nature of the trajectories of tritium ions through the

measured magnetic fields, first to determine their position of impact with the beam dump, and secondly to estimate the distribution of power density on that dump. The latter is an issue because of the focussing effect of the fringe fields of the deflection magnet. This paper describes the techniques that have been used to accomplish these ends.

2. The magnetic field representation

The deflection magnet of the neutral beam injection system is quite complicated and considerable effort has been required for its physics design [3] and manufacture [4]. These details are fortunately of no present concern, because the hardware already exists and the task here is the measurement of its performance in the proposed operating regime.

The magnet coil current required for the present case of 160 keV tritium follows from that required for 160 keV deuterium (810 A), and the dependence $\rho \propto \sqrt{m}/B$ of the cyclotron radius ρ on mass m and magnetic field B, making use of a calibration curve of measured magnet coil current versus B. This gives a value of approximately 1000 A, which is the value used for all the field measurements described below.

The increased field strength required for tritium leads to an increase in the saturation of parts of the iron circuit of the magnet, and hence an increase in its fringe field. For this reason, coupled with previous [4] experience with ab-initio three-dimensional magnetic field computations, direct measurement was considered to be the most desirable means of ascertaining the field structure in this case.

A crucial requirement of this approach is the means to cast the experimental measurements into a form suitable for numerical trajectory calculations. This problem is solved by the use of the "O'Connell box" computer program due to Wind [5] and developed by O'Connell [6].

The magnetic field in the region of interest is a vacuum field. Each Cartesian component therefore satisfies $\nabla^2 B_i = 0$ and in a rectangular box a general solution may be written down in terms of natural and hyperbolic sines and cosines. Furthermore, if the field is known over the surface of the box, the coefficients occurring in the general solution may be determined uniquely and the analytic solution completed.

The O'Connell box program is an application of this use of surface measurements to fix the behaviour of a Laplacian field throughout a box. However, as a matter of practicality, it uses surface measurements over a uniform grid and therefore yields an analytic representation

based on a truncated eigenfunction expansion. This is equivalent to a least-squares fit to the measured data.

In its original form the O'Connell box program was intended to be used separately on each field component and to produce a three-dimensional array for each field component, from which further values were to be calculated by interpolation. This procedure has the advantage of speed, but raises questions of accuracy that can be answered only by potentially lengthy convergence tests. This difficulty has been avoided in the present work by using three distinct but co-existing copies of the O'Connell synthesis program, one for each component, and calculating the field components at any point directly from their analytic representation. This gives unquestionable accuracy at the expense of very much more computation.

The O'Connell box program has been tested on artificial data derived from the exact (but non-physical) Laplacian function $B_i = 1/R$, in which R is the spherical radius from an origin outside the box. In this case, the typical relative error in the synthesized field is 10^{-6} for 10 measurement points along each edge.

3. The magnetic measurements

A complication of the calculation is the need to represent the magnetic field in an L-shaped region. This is achieved by using two separate O'Connell box systems, of which only one is used at any one time.

Figure 1 shows the outline of the deflection magnet and the beam dump, and the layout of the two O'Connell boxes with their sub-division for measuring purposes, discussed below. Both boxes have surface measurements of field at intervals of 0.04 m on all six faces.

The first box covers the region of entry of the trajectories and the greater part of the area covered by the deflection magnet. This box has dimensions $L_x = 2.24$, $L_y = 1.44$, $L_z = 0.16$, corresponding to a grid of $N_x = 57$, $N_y = 37$, $N_z = 5$. Here, L is the length of a side and N the number of grid points along it. All lengths are in metres.

The second box, overlapping the first, covers the exit region of the trajectories and their intersection with the ion dump. This box has $L_x = 1.12$, $L_y = 1.52$, $L_z = 0.16$, corresponding to a grid of $N_x = 29$, $N_y = 39$, $N_z = 5$.

The deflection magnet is intended to be symmetric about $z = 0$ and is known to achieve this to a very good approximation. For present purposes the principal field component B_z is therefore assumed to be exactly symmetric, while the fringe components B_x and B_y are

assumed to be exactly antisymmetric. Accordingly, raw field measurements were taken only in the three planes $z = 0$, $z = 0.04$, $z = 0.08$, and these reflected into negative z by software to give the total of 5 grid points. This is also the minimum number allowed by the O'Connell box program itself.

The measurements of magnetic field were made with a Hall probe mounted on a carriage controlled by stepping motors, and the data captured by microcomputer and written to floppy disk. A complication arose from the limited movement of the probe (0.96 m × 0.56 m, a 25 × 15 grid), which therefore did not permit all the measurements to be taken in a single sequence. Instead, the first O'Connell box was assembled from six measuring boxes and the second O'Connell box from two. The data from each measuring box for each field component consisted of a full set of 25 × 15 values taken at $z = 0.08$ and up to 76 values taken around its sides at $z = 0.04$ and $z = 0$ (for B_z only). Several hundred man-hours were involved in aligning the boxes and taking the measurements, which amounted to more than 10,000 values.

Following the completion of the magnetic measurements, the next steps were to combine the raw data from measuring boxes 1–6 to give the raw data for the first O'Connell box, to check the continuity of this assembled data, and to check its consistency with the magnet current. Figure 2 shows a typical plot of the raw B_y data as a function of x at $y = 0.732$ across the magnet region. This reveals a small residual discontinuity of 8%, a systematic measuring error.

A further complication was that field measurements were not made in two corners of the first O'Connell box (see fig. 3), on the assumption that the values could be taken as zero. In fact, the fields in these unmeasured regions were subsequently inferred to be much larger ($B_z \approx 3 \times 10^{-3}$ T, 1.5% of its central value), and a more accurate approximation was sought. To this end, *artificial* raw field data were generated for these regions by solving Laplace's equation numerically throughout the box, using measured values as immutable Dirichlet boundary conditions and assuming Neumann boundary conditions elsewhere. This procedure served to reduce the field discontinuities to a low level ($\approx 10^{-4}$ T), although it must be said that these localized corrections probably have little effect in practice.

A final check on the integrity of the raw data is provided by contour plots of the field values over each face of the O'Connell box. Figure 3 shows such a plot for B_y in the plane $z = 0.08$ of the first box and demonstrates continuity across the six measuring boxes.

The second O'Connell box is constructed from two measuring boxes and part of the

first O'Connell box. This overlap of the two boxes simplifies the continuation of trajectories from the first box into the second.

Following the assembly and validation of the raw magnetic field data, the last step was to test the *analytic* field generated from it by the O'Connell synthesis program.

Figure 4 shows the analytic representation of B_x, B_y and B_z, plotted across a diagonal of the first O'Connell box. The regions of fringe field and the central region of near-uniform B_z with value 0.2 T are as expected.

Figures 5 and 6 show $\nabla \cdot \mathbf{B}$ and $(\nabla \times \mathbf{B})_x$ respectively, which should be identically zero, plotted across the same diagonal. The field derivatives were calculated from second-order finite differences of the analytic field values. Cancellation of the constituent terms, to about 5%, shows that the synthesized fields do indeed satisfy Maxwell's equations. This provides the ultimate test of correctness of the extensive data acquisition and data processing that underlies this work.

4. The ion trajectories

For the present case of non-relativistic ions and negligible space-charge, the ion trajectories are calculated from the equation of motion

$$\frac{d\mathbf{v}}{dt} = (q/m)\,\mathbf{v} \times \mathbf{B},$$

in which $\mathbf{v}$ is the velocity and q/m is the ratio of charge to mass. Approximate values for tritium are $q/m = 3.2 \times 10^7\,\mathrm{C/kg}$ and $v = 3.2 \times 10^6\,\mathrm{m/s}$ at 160 keV. The values of magnetic field $\mathbf{B}$ are provided by the O'Connell box program described above.

These equations are solved using an 8th order Runge-Kutta scheme due to Butcher [7]. This method allows large steps to be taken with high accuracy. Sub-division of each integration step for plotting or other purposes is provided at minimal extra computational cost by 7th order Hermite interpolation.

The integration routine itself has been tested here on the analytic case of a cyclotron orbit in a uniform magnetic field. Figure 7 shows a log-log plot of the relative error $\Delta x/\rho$ in the computed orbit versus the normalized time-step $\omega \Delta t$ (ρ is the cyclotron radius and ω the cyclotron frequency). This error appears on the graph as a line of gradient 8, thus confirming its scaling as $(\Delta t)^8$ and demonstrating the integrity of the routine.

A complication of the calculation is that the trajectories are split across the two separate O'Connell boxes. Accordingly, all trajectories are first followed in the first O'Connell box,

terminated near its upper-most face ($y = 1.532$), and their last positions used to generate the input data for the continuation run in the second O'Connell box. Transformations are performed between local coordinates in each box (the coordinates in which the calculations are performed) and global coordinates in which the trajectory data are stored on disk for subsequent processing.

The time-step used in the trajectory calculations has to be specified at the outset and a convergence test was performed to determine an appropriate value. Briefly, this showed that as the time-step was decreased below 50 ns, the numerical errors began to fall rapidly and at 20 ns the trajectories showed consistency to a few mm. The value of 20 ns was therefore chosen for all the calculations described below. Hermite interpolation is used to insert 5 extra points per step, to give a final spacing of 10 mm and roughly 200 points on each trajectory.

The number and initial positions of trajectories to be followed through the deflection magnet are chosen according to the application. At the fundamental level, the load on the beam dump depends on the emittance properties of the 262 beamlets that make up the extraction area (of dimensions 0.18 m × 0.45 m) of each of two ion sources. Although the explicit treatment of these beamlets might be feasible, the more practical approach adopted here, following ref. 3, is to represent the combined effect of the beamlets of each source by a single envelope characterized by a single direction in space and a power density level measured relative to the centre of the beam.

For the power density calculations in this model, the initial positions of the trajectories are taken to lie on a rectangular grid covering the envelope in the extraction plane and the initial velocities calculated from the given direction of that envelope.

Following ref. 3, the envelope chosen here corresponds to 50% of the central power density. Each ion source is represented by a grid of size $N_y = 30$, $N_z = 10$, restricted to non-negative z owing to symmetry. This gives a total of 600 trajectories to be followed. A separate computer program is used to generate and verify the necessary initial data.

The production runs, of 600 trajectories each, require 13 hours of computer time per run and are done on a Hitech-10 workstation. This machine gives 1/4 of the processing speed of a CRAY-2 supercomputer for the present (scalar) application, but at greatly reduced cost. The availability of very cheap computing is crucial to the success of the present approach, discussed in section 2, in which field synthesis is used instead of interpolation. Figure 8 shows typical results from the trajectory calculations.

5. The ion dump power density

The ion dump is built from several inverted V-shaped water-cooled copper elements stacked with their vertices along the symmetry line, $z = 0$, of the deflection magnet. There are 12 elements in the proposed design for tritium, each with vertex angle 15° and inclined at 9° to the vertical. The dump is terminated down-stream by an end-plate with a curved scraper at its lower edge.

For present purposes, only the actual beam-impact surfaces are of concern, and these are represented by two plane, two-dimensional, rectangular faces for each element. The end-plate is represented by 8 such faces, to give a total of 32 faces in the computational model.

The first step in the calculation of power density is to find the intersection, if it exists, of each ion trajectory with one of the 32 faces representing the dump. This is done in a simple way by using a series of rotation matrices to transform the faces and the trajectories into standard coordinates, in which the intersections can be easily identified.

Specifically, each face is rotated into some coordinate plane $z' = $ const., and the trajectory data transformed in the same way. The closest trajectory points on either side of this plane are then found and used to calculate the intersection point by quadratic Lagrangian interpolation. Transformation back into the original coordinates then completes the operation. Care is taken to avoid the formation of microscopic holes at the vertices of the elements owing to computer rounding error.

The next step is the calculation of the power density itself. This is accomplished by examining the coordinate mapping associated with the motion of the ions from the source to the dump. A crucial simplifying feature of this mapping is that here it is almost always one-to-one. For this case, if (x, y) are local coordinates in the extraction plane of the ion source and (x', y') are the corresponding local coordinates in a dump face, an element of area $dx\, dy$ in the source maps to an element $J\, dx\, dy$ in the face, in which the Jacobian J is given by

$$J \equiv \frac{\partial(x', y')}{\partial(x, y)}.$$

If the distribution of power density in the source, $p(x, y)$, is known, the corresponding power density on the face is therefore given by

$$p(x', y') = p(x, y)/J.$$

This calculation may be carried through numerically using elements of area of a finite

size. However, a difficulty arises because in general a finite pencil of trajectories will intersect more than one dump face and the calculation of power density then becomes a complicated exercise in solid geometry.

This difficulty has been avoided by the simple expedient of avoiding the general case altogether and calculating the power density only where neighbouring trajectories (as described below), do indeed strike the same dump face. The resolution provided by the 30 × 10 array of trajectories is such that very few areas of the dump are not assigned a power density value by this procedure, which has proved to be extremely practical.

The method of mapping the elements of area is shown in fig. 9. Each grid rectangle in the extraction plane of the ion source is conceptually divided by one of its diagonals into two triangles, and similarly by its other diagonal into another two triangles. Each grid rectangle, and hence each triangle, is mapped by the trajectories at its vertices into the beam dump, as determined by the intersection points calculated above. If, and only if, all three vertices of any mapped triangle are found to lie on the same dump face, its area A_2 is found and the local power density within it calculated from the expression

$$p_2 = p_1 A_1 / A_2,$$

in which A_1 is the area of the same triangle in the extraction plane and p_1 is the known power density there. This procedure is justified because the mapped rectangles do not usually overlap. A further simplification is that for practical purposes the source power density, p_1, may be taken as a constant over the entire extraction plane.

The mathematical meaning of the power density calculated in this intuitive way may be seen by considering the analytic case of a bilinear trajectory mapping, which will be a good local approximation to the real behaviour within each small grid rectangle. In this case it may be easily shown that the four power density values obtained from the four finite triangles are identical to the analytic values in the four corners of the mapped rectangle.

6. Results

Figure 10 shows the regions of impact on the ion dump of 160 keV ions, plotted in a projection onto the x-z plane (i.e., a view vertically into the V-shaped elements). As explained above, it is calculated by mapping the 50% power envelope of each of two ion sources. A favourable feature is that the images of the two sources do not overlap, but an unfavourable feature (not shown) is that there is a load on the end-plate.

The calculation of the power density in the dump requires a value p_1 for the power density in the ion source. This has been taken as 38 MW/m^2, as a worst-case approximation, calculated by assuming that all the ion power (2.25 MW per source) is contained within the 50% contour (of dimensions 0.15 m × 0.39 m).

The results show a systematic increase in power density from typically 2 MW/m^2 at the centre of each beam image to about 6 MW/m^2 at its left and right edges, beyond which it drops to zero abruptly. Power density profiles of this shape were predicted (see fig. 8, ref. 3). They arise from the fact that away from the apex of the V-shaped beam dump, both the angle of incidence of the beam and the beam power density increase as a consequence of the non-bend plane line focus existing inside the magnet.

The sharp cut-off is inherent in the assumption of a top-hat beam profile. This is adequate to calculate the peak power density at the centre of the dump, but obviously breaks down at the beam edge. Exactly at the edge the power density is over-estimated by a factor of 2 (here the top-hat width equals the 50% contour width of the real beam profile), and a more accurate treatment would require a finite beam emittance calculation as was done previously [3]. However, since the power densities fall well within the 10 MW/M^2 limit that the dump elements can dissipate, an emittance calculation was not pursued in this case. Figure 11 shows a magnified view of the elementary triangles used in these calculations.

The calculated load on the end-plate is about 1 MW/m^2, which although undesirable in principle, is nevertheless acceptable in practice. These favourable results suggest that the proposed operation with tritium is indeed feasible.

Figure 12 shows the effect on ion deposition of a reduction in the energy of the beam, which corresponds to an increase in the bending power of the deflection magnet. The energy has been decreased to 152 keV, the lowest value for which the deflected beam from the upper ion source remains within the beam dump. A favourable change is the removal of the load on the end-plate, but this is countered by the appearance of significant lateral (non-bend plane) focussing at the edges along $x = 1.0$ of the image of the upper ion source. The computed maximum power density there is approximately 250 MW/m^2, which far exceeds the capacity of the dump elements.

In view of the sharpness of this focussing, the power density values were themselves subjected to a time-step convergence test. This used eight critical trajectories in the focussing region, the limited number making practical the use of time-steps down to 1 ns. Figure 13 shows the results obtained from this study. Although there are fluctuations even at small

values of time-step (these have not been explored, but may arise from interpolation error), the results are consistent to 6%.

The appearance of the second non-bend plane focus at high magnetic field settings, or alternatively, low ion beam energies was predicted [3] and is an inherent limitation of the magnet ion optics that is aggravated at high magnetic saturation levels as is the case for tritium operation.

Although the sharp focussing is a very localized phenomenon ($\approx$ 10 mm width), and will be blurred to an estimated 100 MW/m^2 when taking into account the finite beam emittance, the results strongly suggest that operation with too low an ion energy or too high a magnet current setting will cause localized damage to the dump. This effect has indeed been observed during hydrogen operation in the JET test-bed [1].

7. Summary

Numerical ion optics calculations have been performed to determine the feasibility of tritium injection into JET, using the existing design of ion deflection magnet.

The magnetic field of the deflection magnet has been represented analytically by a solution of Laplace's equation based on extensive field measurements.

The distribution of power density in the ion dump has been calculated by mapping an array of 600 ion trajectories from the ion source.

The maximum power density for 160 keV tritium is calculated to be 6 MW/m^2, well within the capacity of the dump elements. The use of too low a beam energy, or too high a magnet current setting, may lead to sharp focussing and regions of unacceptably high power density.

Acknowledgements

References

[1] H.D. Falter, R.S. Hemsworth, G.H. Deschamps, A.P.H. Goede, T.T.C. Jones, P. Massmann, M.J. Mead, Proc. 11th Symp. Fusion Engineering, Austin, Texas (1985), IEEE Publ. No. 2251-7, Vol. 2, pp. 786-790.

[2] A.P.H. Goede and H.D. Falter, Proc. 7th Int. Conf. High Power Particle Beams, Karlsruhe (1988), Vol. 1, p. 747. Ed. W. Bauer and W. Schmidt, Kernforschungszentrum Karlsruhe GmbH, ISBN 3-923704-01-1.

[3] A.P.H. Goede, B.R. Nielsen and E. Thompson, Nucl. Inst. and Meth. A267 (1988) 193.

[4] A.P.H. Goede, B.R. Nielsen, F. Shone, T. Sønderskov and E. Thompson, Nucl. Inst. and Meth. A267 (1988) 203.

[5] H. Wind, Nucl. Inst. and Meth. 84 (1970) 117.

[6] M.J. O'Connell, Comput. Phys. Comm. 11 (1976) 221.

[7] J.C. Butcher, J. Ass. Comput. Mach. 14 (1967) 84.
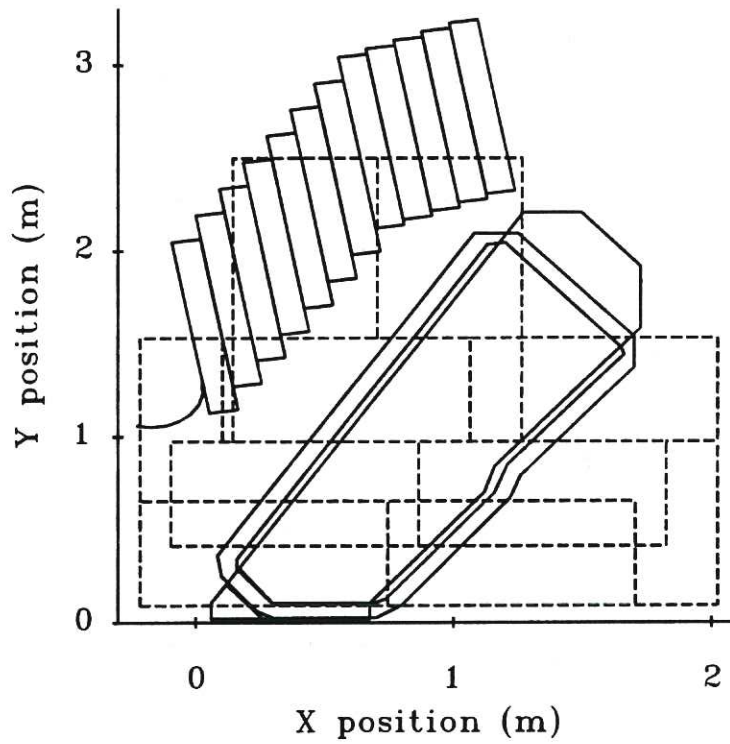
Figure 1

This shows a side view of the deflection magnet (the central structure), and the ion beam dump above it. The dashed lines indicate the layout of the two O'Connell boxes and their sub-division for measuring purposes. Box 1 is defined by $-0.2156 \leq x \leq 2.0244$, $0.092 \leq y \leq 1.532$. Box 2 is defined by $0.1444 \leq x \leq 1.2644$, $0.972 \leq y \leq 2.492$.
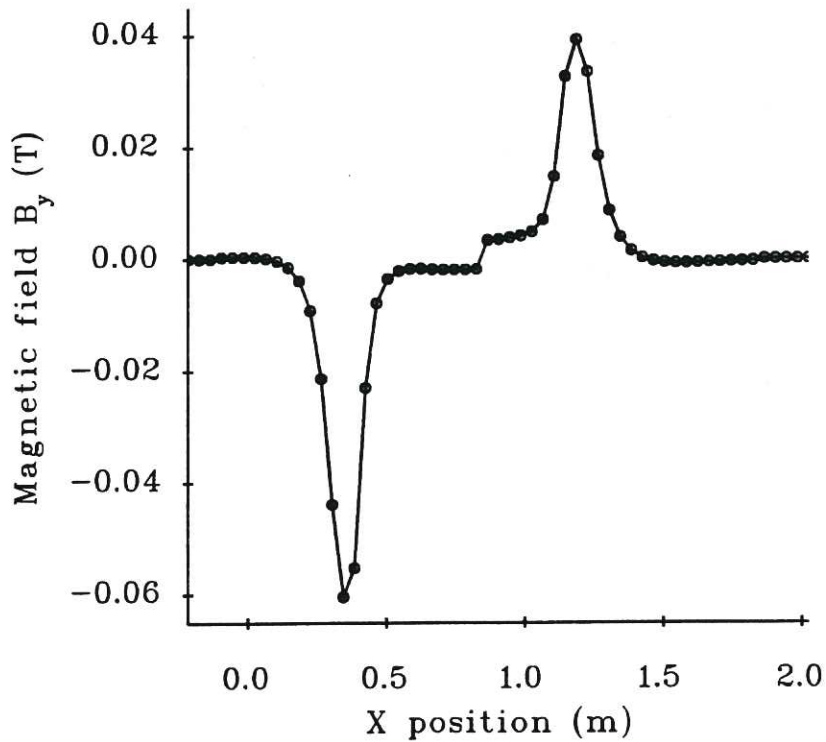
Figure 2

This shows a plot of the raw B_y data as a function of x at $y = 0.732$. The peaks are consistent with the direction of current in the magnet coils, but there is an 8% discontinuity at $x = 0.86$ arising from measuring error.
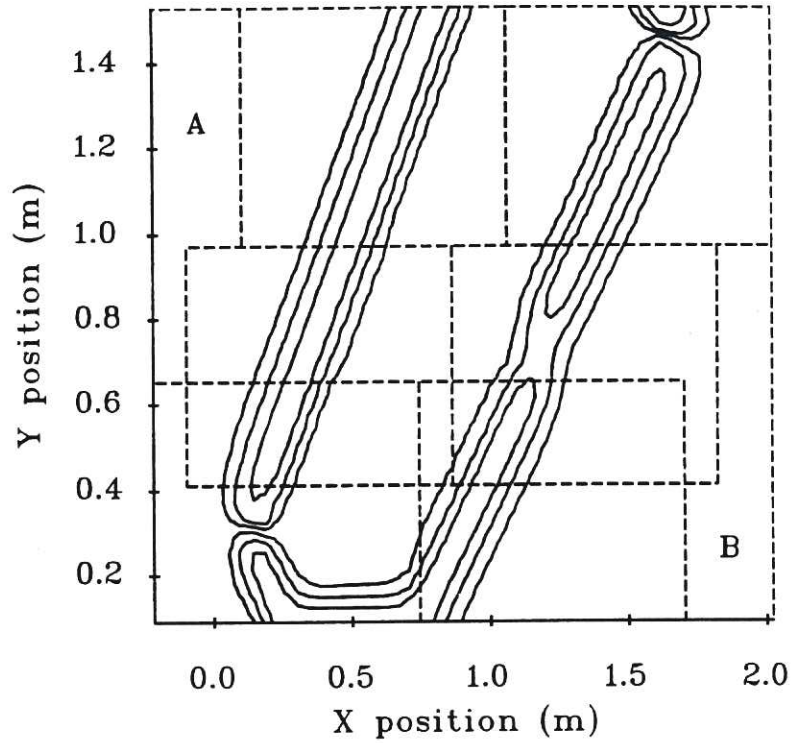
Figure 3

This shows a contour plot of the raw B_y data in the plane $z = 0.08$ of the first O'Connell box, and demonstrates continuity across the six measuring boxes. The L-shaped regions A and B contain the artificial Laplacian data described in the text.
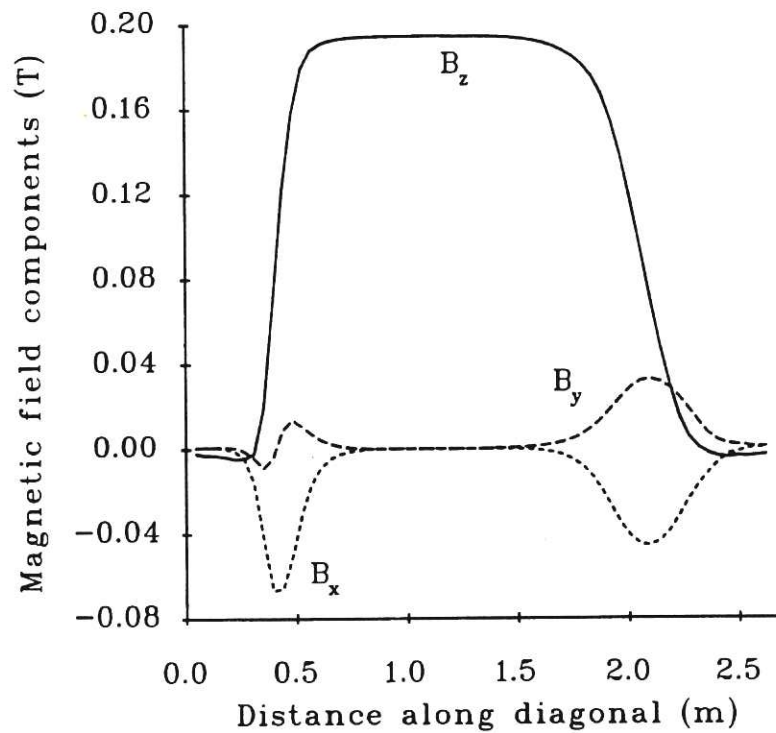
Figure 4

This shows the synthesized magnetic field components plotted across a diagonal of the first O'Connell box. The regions of fringe field (B_x and B_y), and the central region of uniform B_z are as expected.
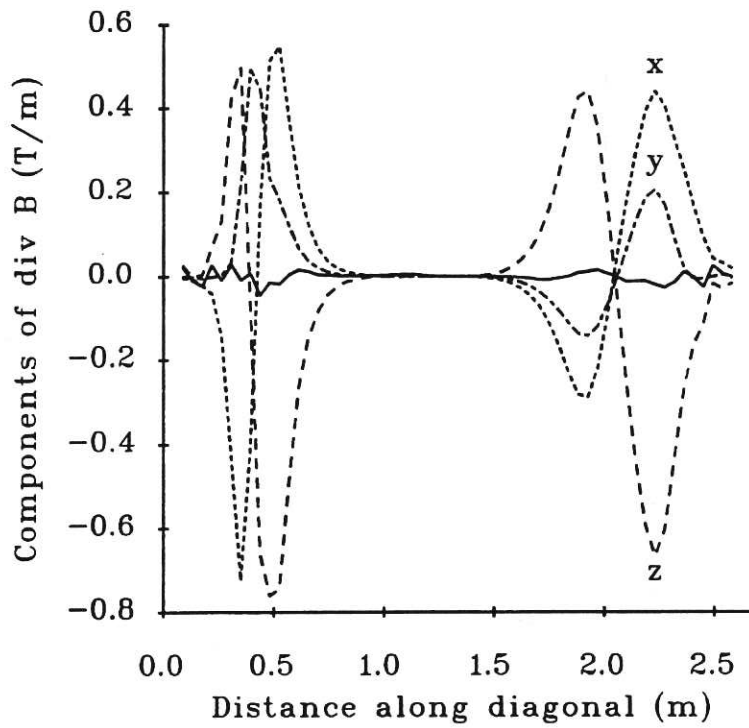
Figure 5

This shows $\nabla \cdot \mathbf{B}$ and its constituent terms, calculated from finite differences of the synthe-sized field, and plotted across a diagonal of the first O'Connell box. The three dashed lines x, y and z refer to $\partial B_x/\partial x$, $\partial B_y/\partial y$ and $\partial B_z/\partial z$ respectively. The solid line, close to zero, is the resultant value of $\nabla \cdot \mathbf{B}$.
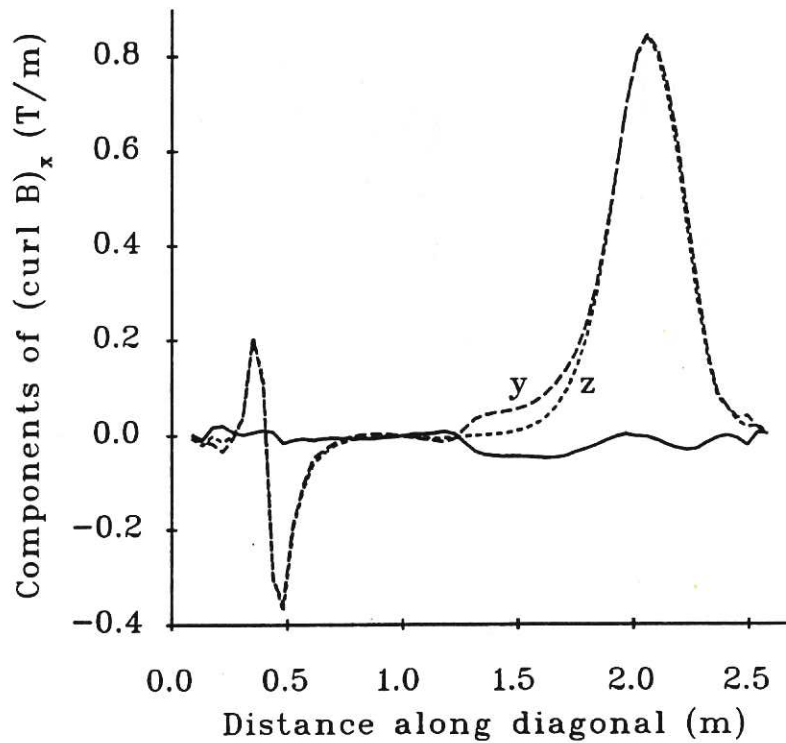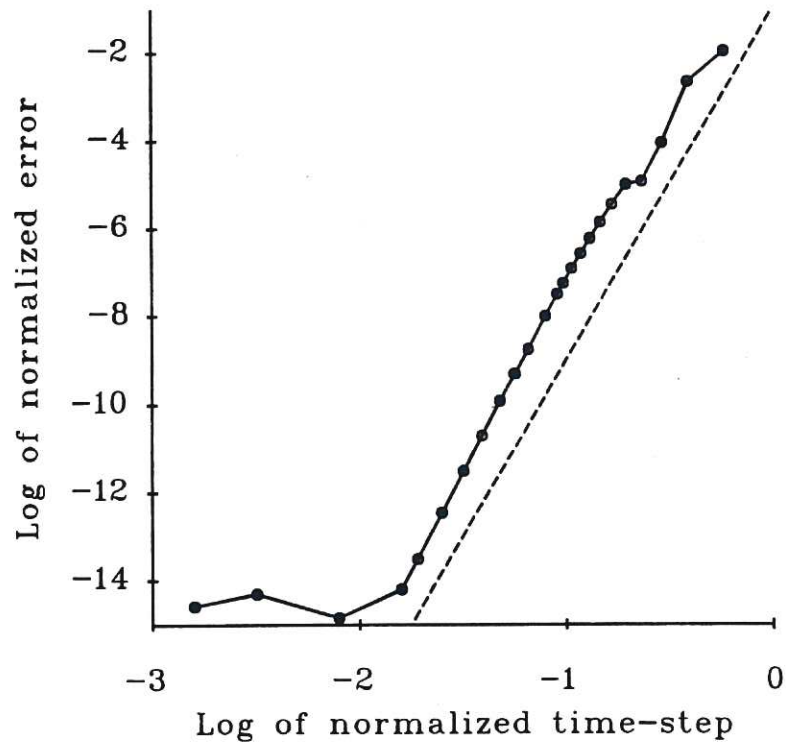

Figure 6

This shows $(\nabla \times \mathbf{B})_x$ and its constituent terms, calculated from finite differences of the synthesized field, and plotted across a diagonal of the first O'Connell box. The two dashed lines y and z refer to $\partial B_y/\partial z$ and $\partial B_z/\partial y$ respectively. The solid line, close to zero, is the resultant value of $(\nabla \times \mathbf{B})_x$.

Figure 7

This shows the results of the integration accuracy test for the case of a cyclotron orbit. $\log_{10}$ of the normalized error is plotted against $\log_{10}$ of the normalized time-step and is compared with the theoretical scaling line of gradient 8, shown dashed.
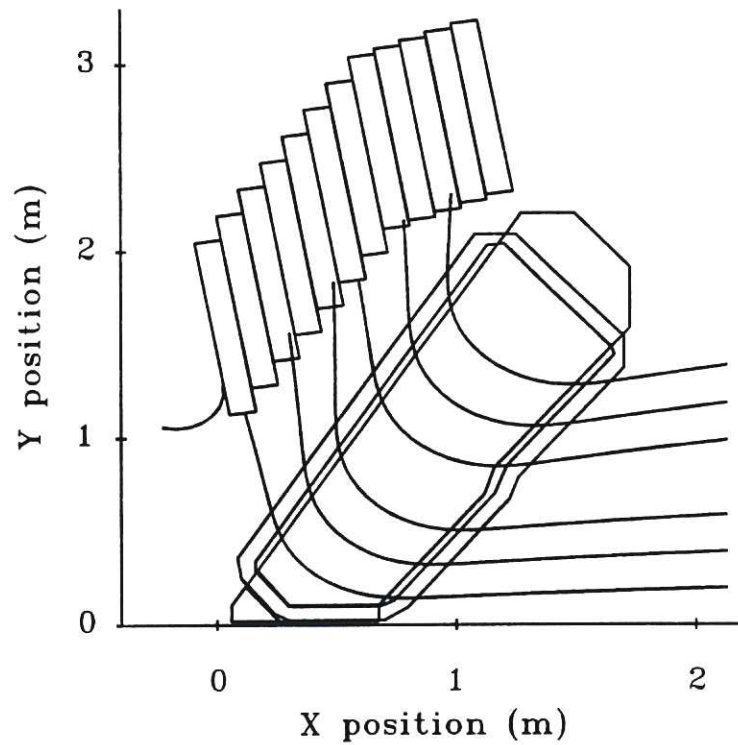

Figure 8

This shows typical results from the trajectory calculations. The ions enter from the right-hand side and are deflected vertically into the beam dump. Three rays are shown from each of the two ion sources.
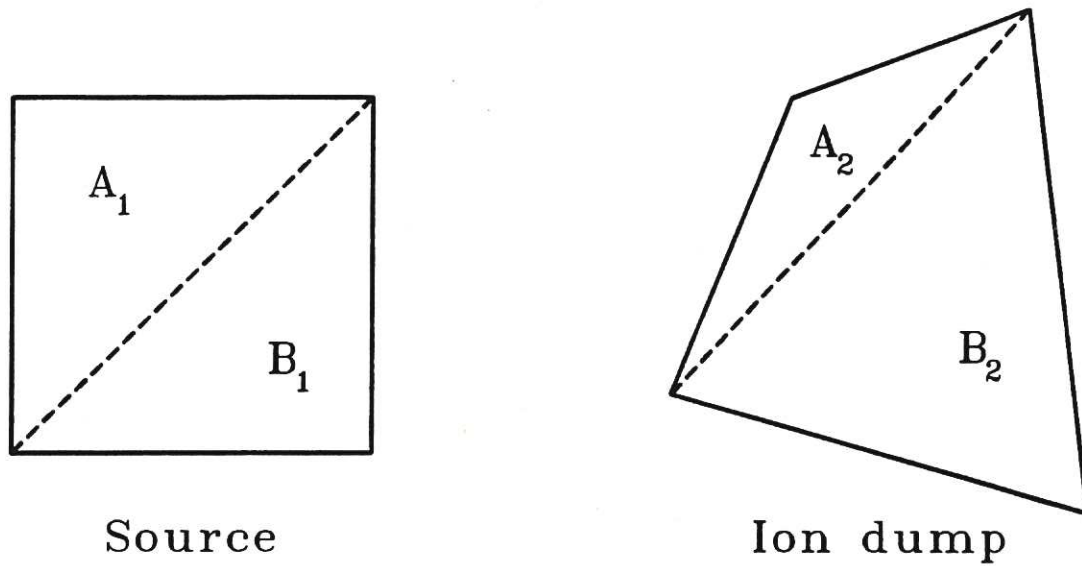
Source   Ion dump

Figure 9

This shows the method of mapping the elements of area used in the power density calcula-
tions. Triangles A_1 and B_1 in the ion source map into triangles A_2 and B_2 in the ion dump,
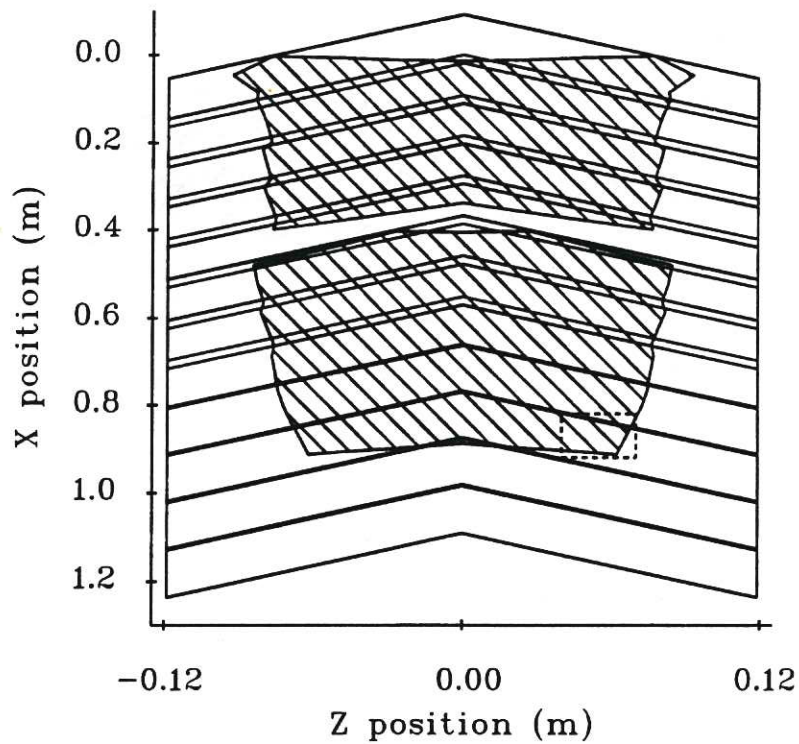and the power density calculated from the ratio of areas.

Figure 10

This shows the regions of impact on the ion dump of 160 keV ions from the two ion sources,
plotted in a projection onto the z-z plane. A magnified view of the boxed region is shown
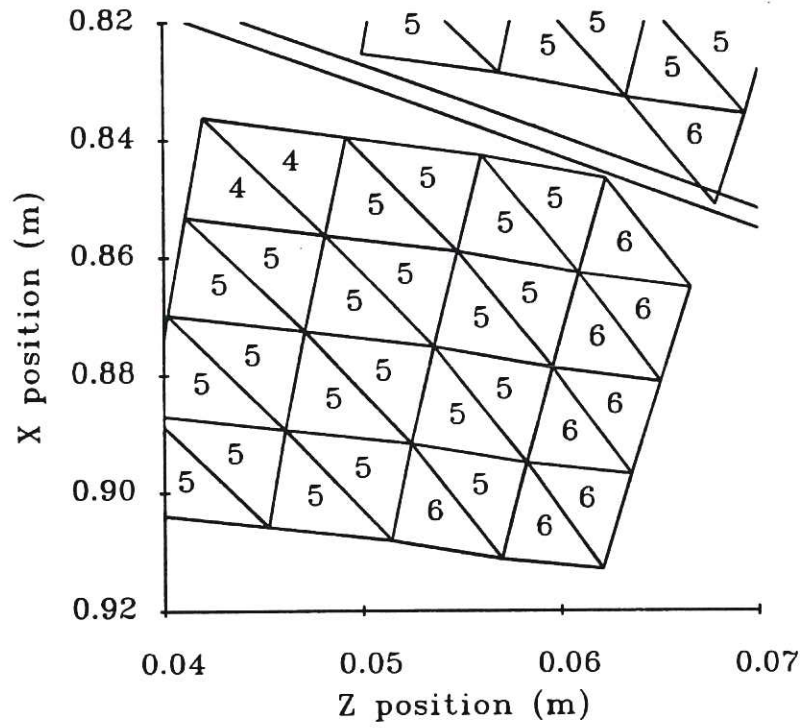in figure 11.

Figure 11

This shows a magnified view of the region of the ion dump outlined in figure 10, and displays the triangular elements of area. Each triangle is annotated with the local power density in MW/m².
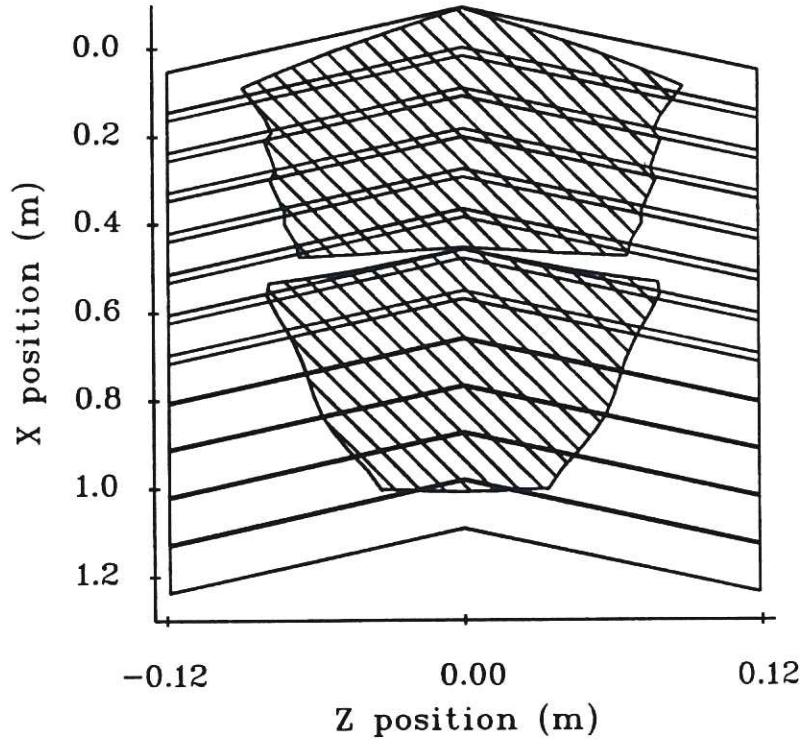

Figure 12

This shows the regions of impact on the ion dump of 152 keV ions from the two ion sources, plotted in a projection onto the x-z plane. The most significant difference from figure 10 is the strong lateral focussing at $x = 1.0$.
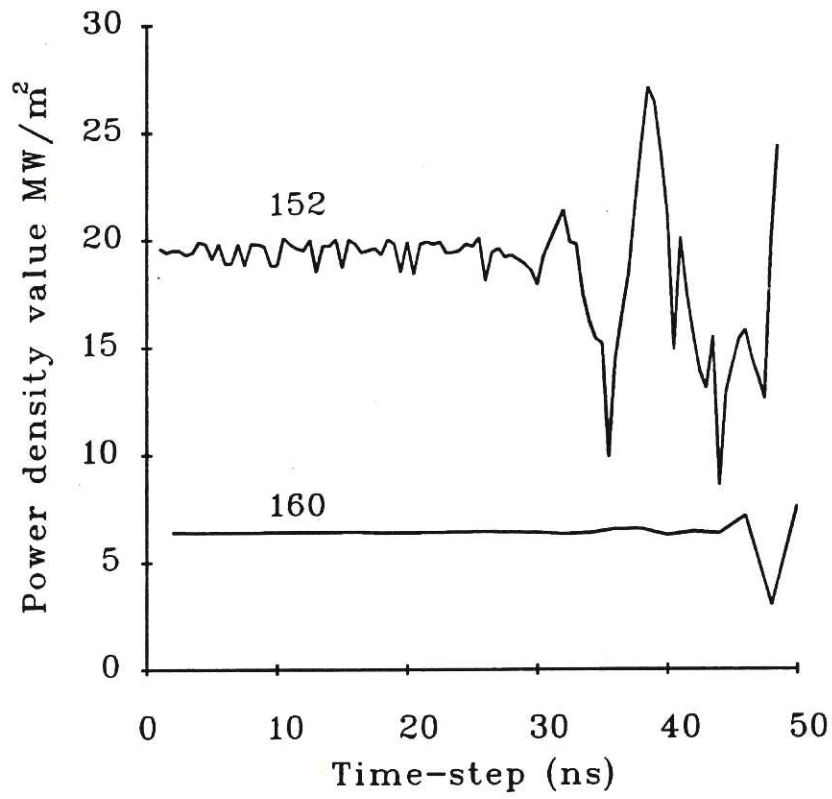
Figure 13

This shows the results of the trajectory time-step convergence test on the computed ion dump power density. Below 25 ns, the results for 152 keV and 160 keV show fluctuations of 6% and 0.4% respectively. The time-step for production runs is 20 ns.